Tower, B. (1885), 'Second Report on Friction Experiments (Experiments on Oil Pressure in a Bearing)', *Proc Inst Mech Eng*, 58–70.

Yang, D. and Liu, Y. (2008), 'Numerical simulation of electroosmotic flow in microchannels with sinusoidal roughness', *Colloids and Surfaces A: Physicochem. Eng. Aspects* 328(1–3): 28–33.

Micro/nano tribology

K. Mylvaganam and L. C. Zhang, University of New South Wales, Australia

Abstract: This chapter discusses the micro/nano sliding of materials in terms of adhesion, wear, friction and lubrication, using both experimental and theoretical methods such as SFA, STM, AFM, FFM and molecular dynamics simulation. A focus is to understand some characteristic phenomena associated with micro/nano tribology such as the scale effect of friction and wear deformation transition on no-wear, adhesion, ploughing and cutting regimes.

Keywords: adhesion, wear, friction, lubrication, molecular dynamics.

4.1 Introduction

Micro/nano tribology concerns the friction and wear of two objects in relative sliding whose dimensions range from micro-scales down to molecular and atomic scales. Unlike macro-tribology in which wear is inevitable, in micro/nano tribology wear is very light and the properties of contact surfaces often dominate the tribological performance.

It has been found that the adhesion force of a micro-scale object is over a million times greater than the force of gravity. This is because the adhesion force decreases linearly with size, whereas the gravitational force decreases with the size cubed (Kendall, 1994). Thus, micro objects adhere to their neighbours or surfaces and this is an obstacle to the miniaturization of components. Reduction in adhesion and friction were realized by applying principles of surface chemistry and tribology to micro-electromechanical systems (MEMS) that have a characteristic length of 100 nm to 1 mm, and nano-electromechanical systems (NEMS) that have a characteristic length of less than 100 nm. Contemporary examples in which atomic friction and wear play a central role are the optimal design, fabrication and operation of devices with atomic resolution, such as micro-machines and high-density magnetic recording systems. Over the last two decades or so, many studies have been carried out to explore the mechanisms of nano-friction and nano-wear, both theoretically and experimentally.

In this chapter we will discuss the micro/nano tribological investigations using surface force apparatus (SFA), scanning tunnelling microscope (STM), and atomic force microscopy (AFM) as well as friction force microscopy (FFM) (a subsequent modification of AFM). We will then present an overview on the capability of various methods for theoretical investigations. The molecular dynamics modelling to characterize the nanodeformation mechanisms will be demonstrated using diamond-copper and diamond-silicon systems as examples.

4.2 Experimental investigation

The study of tribology at micron and nanometre scales has become experimentally possible with the invention of SFA,

STM, AFM and FFM. Although all these are small-scale techniques, their measurement capabilities are different. For example, the SFA measures the interaction between molecularly smooth surfaces separated by a thin lubricant film; with which the surface separation, area of contact, lateral forces, and normal forces can be simultaneously measured. However, the AFM brings a sharp tip into contact with a lubricated surface, in which the film thickness and exact area of contact are unknown, while measuring the lateral and normal forces. Furthermore, the magnitude of the applied load, size of the contact area, and the composition of the probe surfaces in the above techniques are different. Table 4.1 compares some features of the SFA, STM and AFM techniques.

4.2.1 SFA analysis

The SFA developed in 1968 (Tabor and Winterton, 1969) and improved by Israelachvili and Tabor (Israelachvili and Tabor, 1972) is a common tool in the study of both static and dynamic properties of molecularly thin films sandwiched

Table 4.1 Comparison of some features of SFA, STM and AFM

Parameters	SFA	STM	AFM
Applied load	1–200 mN	N/A	1–100 nN
Size of the contact area	~10^{-5} cm^2	N/A	~10^{-13} cm^2
Sliding velocity	0.5–5 μm/s	0.02–200 μm/s	0–200 μm/s
Probe	Mica (generally)	Tungsten	Si_3N_4/Si/ diamond
Substrate requirement	Atomically smooth	Electrically conducting	Any

between two molecularly smooth surfaces. In the SFA, which comprises crossed cylinders of atomically smooth cleaved mica, the sliding friction force, surface separation and the area of contact can be measured simultaneously for a range of loads. The principal tribological application has been to study boundary lubrication with films a few molecules thick, although several friction measurements with dry surfaces have also been carried out.

A direct measurement of van der Waals forces in air between sheets of mica was made by accurately measuring the separation using multiple beam interferometry with an accuracy of ±0.3 nm (Tabor and Winterton, 1969). In this experiment one surface was held on a rigid support and the other on a light cantilever beam. As the surfaces were brought together, at a certain separation the surfaces jump into contact ('flick' together) when the attractive force between the surfaces overcomes the stiffness of the spring. Thus the 'flick' distance depends on the stiffness of the cantilever and this in turn provides a direct measure of the surface forces. Tabor and Winterton showed that 'normal' van der Waals forces predominate for separations less than 10 nm and the 'retarded' forces operate for distances greater than 20 nm.

Homola and co-workers (Homola et al., 1990) used SFA for simultaneous measurements of both the normal and the frictional forces between two molecularly smooth surfaces, the exact molecular contact area of the surfaces, the surface profile during sliding, and the distance between the two surfaces. They studied the sliding of mica surfaces in (i) dry atmosphere, (ii) controlled vapour atmospheres (i.e. in air or N_2), and (iii) with the surfaces immersed in bulk liquids. The interaction forces associated with this interfacial sliding was found to be much more localized than in the case of normal friction or boundary lubrication where the two surfaces separated by thin layers of some lubricant in which plastic

deformations and damage occur during sliding. The work showed that at low loads the frictional force is described by the equation originally proposed by Bowden and Tabor: $F=S_cA$, where A is the molecular contact area and S_c is the critical shear stress (Bowden and Tabor, 1967). It was found that the dependence of A on the load is well described by the JKR theory (for adhesive contacts) and the Hertz theory (for non-adhesive contacts) even during sliding. At higher loads, adhesion is destroyed, multiasperity contact is established and the frictional force (F) becomes proportional to the load (L), analogous to Amontons' law, $F=\mu L$. In the presence of water vapour the friction decreased but the area of contact did not change, showing that the adhesion was maintained.

4.2.2 STM studies

The pioneering work on surface topography obtained with STM was published in 1982 by Binning and co-workers. In STM a sharp tip was systematically scanned over a sample surface in order to obtain information on the tip-sample interaction down to the atomic scale. As it used the tunnelling current between the conducting tip and a conducting sample, thus named the 'scanning tunnelling microscope', STM can only be used to study surfaces which are electrically conductive to some degree.

Since its invention, STM has provided images of surfaces and absorbed atoms and molecules with unprecedented resolution (Binning et al., 1982, Becker et al., 1985). An experimental result on surface topography was obtained in 1982 in which the surface reconstructions for (1 1 0) surfaces of $CaIrSn_4$ and Au were shown. The very high resolution of the STM rests on the strong dependence of the tunnel current on the distance between the metal tip and the scanned surface. STM has also been used to modify surfaces by

locally pinning molecules to a surface (Foster et al., 1988) and by the transfer of an atom from the STM tip to the surface (Eigler and Schweizer, 1990). The tip of an STM exerts a finite force, which contains both van der Waals and electrostatic contributions, on an atom. Hence the magnitude and the direction of this force may be tuned by adjusting the position and the voltage of the tip. In addition, generally less force is required to move an atom along the surface than to pull it away from the surface. Thus it is possible to set the parameters such that the tip can pull an atom across the surface while the atom remains bound to the surface. For example, Eigler and Schweizer positioned xenon atoms on a single-crystal nickel surface with atomic precision by first placing the tip above the xenon atom and then increasing the tip–atom interaction by changing the required tunnel current to a higher value, which caused the tip to move towards the atom. They then moved the tip across the surface to the desired destination, dragging the xenon atoms. The tunnel current was then reduced to terminate the attraction between xenon and the tip, leaving the xenon bound to the surface at the desired location.

4.2.3 AFM and FFM investigations

The atomic force microscope introduced in 1985 (Binnig et al., 1986) provided a method for measuring forces on a nano-scale between a probe tip and an engineering surface. The AFM typically uses sharp silicon nitride, silicon, or diamond probes, whereas no specific chemistry is required for the substrate surface. The tip is attached to a free end of a cantilever and is brought very close to the surface. The cantilever bends towards or away from the sample in response to attractive or repulsive forces and its deflection is detected by means of a laser beam which is proportional to the normal force applied to the tip. AFM can operate in contact mode and non-contact mode. In the contact mode, the tip makes soft physical contact of the sample and either scans at a constant height or under a constant force where the deflection of the cantilever is fixed; even atomic resolution images are obtained in this mode. In the non-contact mode, the tip operates in the attractive force region and the tip-sample interaction is minimized. This mode allows scanning and the cantilever of choice is the one having a high spring constant so that it does not stick to the sample surface at small amplitudes.

Unlike STM, AFM has been used for topographical measurements of surfaces on the nanoscale which may be either electrically conducting or insulating as well as measuring adhesion and electrostatic force. Localized deformation, tip-substrate interactions and environmental effects often make the results difficult to reproduce. In 1987, a research group (Mate et al., 1987) at IBM reported an observation where the atomic structure of a surface manifests itself directly in the dynamical frictional properties of an interface. In particular, when they slide a tungsten tip on the basal plane of graphite, they observed that the frictional force displayed atomic periodicity of the graphite surface. According to them the friction coefficient between a tungsten tip of radius 300 nm and a basal plane of a graphite grain was 0.012 at a normal load of 10 μN. Another early interesting study (Kaneko et al., 1988) on the sliding of a tungsten tip of radius 10 μm on a carbon sputtered surface measured frictional force of about 1 μN at zero normal force, indicating an infinite friction coefficient.

Subsequent modification of AFM led to the development of the Friction Force Microscope (FFM) which is used to measure forces in the scanning direction, i.e. the force of friction. An AFM/FFM tip sliding on a surface simulates

just one contact whereas at most solid–solid interfaces contact occurs at many asperities. Even so, as these asperities are of different sizes and shapes, the effect of size on friction/adhesion can be studied using tips of different radii. Bhushan and his co-workers have used these instruments to study various tribological phenomena such as surface roughness, adhesion, friction, scratching, wear, detection of material transition, etc. (Bhushan and Ruan, 1994; Ruan and Bhushan, 1994; Bhushan, 1995; Koinkar and Bhushan, 1997; Zhao and Bhushan, 1998; Sundararajan and Bhushan, 2000; Bhushan and Sundararajan, 1998; Bhushan and Dandavate, 2000). For example, Ruan and Bhushan used FFM to study a freshly cleaved highly-oriented pyrolytic graphite (HOPG) surface and found that the atomic-scale friction and the topography exhibited the same periodicity but the peaks were displaced relative to each other, which was explained by the variation in interatomic force in the normal and lateral directions. In a different study (Ruan and Bhushan, 1994) the same authors have reported that the coefficient of nano-scale friction for a Si_3N_4 tip of radius 50 nm versus HOPG graphite, natural diamond and Si(100) are 0.006, 0.04 and 0.07 respectively compared to the macro scale values of 0.1, 0.2 and 0.4. Recently, Bhushan presented a comprehensive review of AFM/FFM studies on the significant aspects of nano-tribology, nano-mechanics and material characterization (Bhushan, 2005).

McGuiggan and co-workers compared the AFM measurements with SFA measurements and found that for two different thin polymer films, AFM results showed little difference in the friction whereas SFA results gave a large difference (McGuiggan et al., 2001). This was explained by the variations in size of the probe of AFM and SFA. The sharp AFM tip may penetrate the lubricant film leading to the tip contacting, at least partially, the substrate surface.

One then measures the friction between two solid surfaces and the lubricant has little effect. On the other hand, SFA with its large contact area (see Table 4.1) maintained a uniform film thickness between the probe and the surface. Hence in this case, differences in the friction measurements may be due to differences in the film thickness.

The above experimental investigations demonstrate that the tribological properties such as surface roughness, adhesion, friction, wear, detection of material transfer and boundary lubrication can be studied at the micro/nano scale. However, to understand any discrepancies emerging from the different experimental methods, and to properly characterize the deformation mechanisms during the micro/nano tribological processes, theoretical methods are often required.

4.3 Theoretical investigation

4.3.1 Introduction

The advent of super computers for large-scale atomic simulations has led to the development of computational micro- and nano-tribology. While quantum mechanics is ideal for very small models on the atomic scale and micro/continuum mechanics is powerful for analysing the objects of micro and macroscopic dimensions, molecular dynamics (MD) simulation provides a useful means for detailed characterization of materials on the nano scale. However, the small time steps used in these simulations tend to result in a sliding speed far exceeding that in physical reality. The advantage of using molecular dynamics lies in its capacity to handle relatively large molecular systems; this is hard to do using quantum mechanics. Hence the reliability of molecular dynamics in exploring atomistic deformation mechanisms

such as phase transformations and dislocation emissions – to which micromechanics and continuum mechanics are not applicable. Thus, MD simulations provide useful insight into experimental observations that may lead to the discovery of new phenomena or act as drivers for new experiments that in turn may lead to an eventual solution to the engineering problems in tribology. Moreover, 3D-computer visualization and animation allow us to follow atomistic behaviour during simulation at different time steps that helps to understand the chemistry and mechanics of the processes.

The MD simulation of nano-deformation operations depends on a number of essential modelling factors such as the choice of atomic interaction potential, the generation of the initial molecular model of the material and its relaxation process, the control of simulation temperature, the selection of control volume size and the application of moving control volume technique, the determination of integration time steps, identification of a temperature conversion model, and the method of stress analysis. For a discussion on these important issues in studying the nano-tribology using molecular dynamics the readers may refer to Zhang and Tanaka (1998, 1999) and Cheong et al. (2001).

As stated in section 4.2.1, the importance of the atomic contact area to atomic friction is not difficult to understand if the JKR theory is recalled. This theory, while considering the effect of surface energy in its analysis, has implicitly indicated that the real contact area must be of great concern to sliding loads on the atomic scale. If looking into the details of contact sliding, we can have two primary situations (Zhang and Tanaka, 1998). When two surfaces are in sliding without foreign particles, they are in two-body contact sliding, as shown in Fig. 4.1(a). In this case, the interactions among surface asperities play a central role in the process of wear and friction. However, if some particles appear between

Figure 4.1 Schematic drawing of molecular dynamics modelling of the sliding processes: (a) two-body sliding, (b) three-body sliding

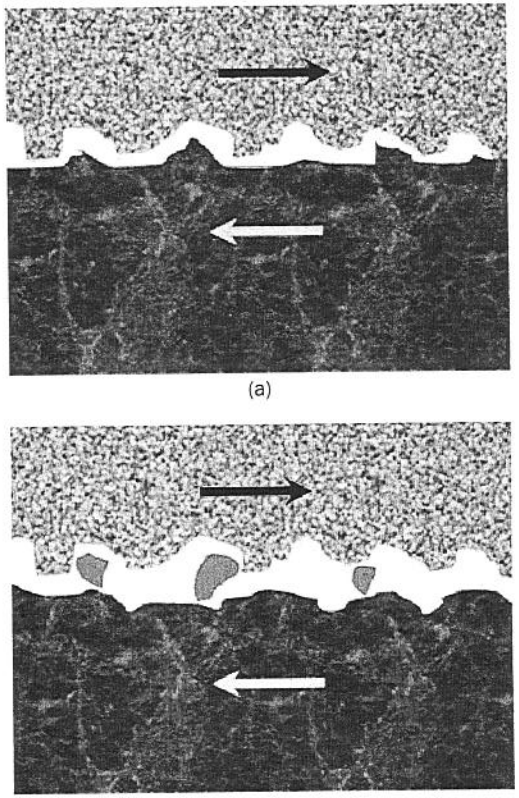

the surfaces, which could be the debris from worn surfaces or foreign particles due to contamination, a three-body contact sliding occurs, as shown in Fig. 4.1(b).

4.3.2 *Diamond-copper sliding systems*

Methods of modelling and analysis

For simplicity, an atomically smooth diamond asperity sliding on an atomically smooth surface of a copper

monocrystal in its (1 1 1) plane has been considered. The variables of interest are the sliding speed V, indentation depth d, degree of surface lubrication or contamination and the tip radius of asperity R which is the radius of the envelope of centres of the surface atoms. The environmental temperature of the sliding system is 293 °K and the asperity rake angle is $-60°$. In addition, it is assumed that d keeps constant in a sliding process, which implies that the sliding system has infinite loop stiffness.

The initial model used in this sliding simulation consisted of a copper monocrystal work piece in its (1 1 1) plane with thermostat atoms arranged around the control volume to conduct the heat out properly and with boundary atoms arranged fixed to the space to eliminate the rigid body motion. A hemispherical diamond was used as the asperity. The interactions between copper–copper and copper–diamond atoms can be described by the modified Morse potential given by

$$\phi(r_{ij}) = \lambda_1 D\left[e^{-2\lambda_2\alpha(r_{ij}-r_0)} - 2e^{\lambda_2\alpha(r_{ij}-r_0)}\right], \qquad [4.1]$$

where r_{ij} is the interatomic separation between atoms i and j and r_0 is the equilibrium separation at which the potential is minimized. D and α are material constants listed in Table 4.2. With the above potential function available, the forces on atom i due to the interaction of all the other atoms can be calculated by

$$F_i = -\sum_{j=1, j\neq i}^{N} \Delta_i \phi\left(r_{ij}\right) \qquad [4.2]$$

where N is the total number of atoms in the model, (12000 <N<15000 is used in conjunction with the technique of moving control volume) including thermostat, boundary and diamond atoms. Consequently, the motion of all the Newtonian atoms in the control volume, including their instant position and velocity vectors, can be obtained by

Table 4.2 Parameters in the standard Morse potential

Parameter	C–Si	Cu–Cu	Cu–C
D (eV)	0.435	0.342	0.087
α (nm^{-1})	46.487	13.59	51.40
r_0 (nm)	0.19475	0.287	0.205
λ_1	1	1	(0,1)
λ_2	1	1	≥1

following the standard procedures of molecular dynamics analysis.

In principle, an asperity is three-dimensional and thus a three-dimensional molecular dynamics analysis would be more appropriate. However, a careful comparison showed (Tanaka and Zhang, 1996) that a two-dimensional model can lead to sufficiently accurate results in terms of the variations of temperature and sliding forces and easier characterization of deformation. We will therefore focus on the two-dimensional, plane-strain analysis in this section. When an instant configuration of the copper atomic lattice during sliding is obtained by the molecular dynamics analysis, the distribution of dislocations in the deformed lattice can be determined by the standard dislocation analysis (Courtney, 1990).

Mechanisms of wear

The deformation of the copper specimen has four distinct regimes under sliding, the no-wear regime, adhering regime, ploughing regime and cutting regime, as shown in Fig. 4.2. In the figure, the transition of deformation regimes is characterized by the non-dimensional indentation depth δ. When contact sliding takes place, δ is defined as d/R and can be viewed as a measure of the strain imposed by the diamond asperity.

Figure 4.2 The transition of no-wear and wear regimes (the diamond slides from right to left)

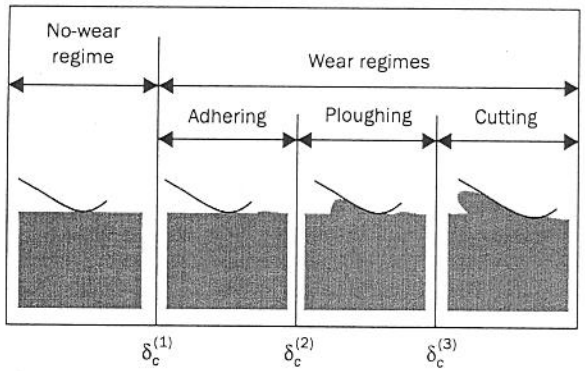

(Reprinted from Zhang and Tanaka (1997) with permission from Elsevier Science.)

In the no-wear regime, the atomic lattice of copper is deformed purely elastically. After the diamond asperity slides over, the deformed lattice recovers completely. In this case, sliding does not introduce any wear or initiate any dislocation.

When δ increases and reaches its first critical value, $\delta_c^{(1)}$, adhering occurs. The atomic bonds of some surface copper atoms are broken by the diamond sliding and these copper atoms then adhere to the asperity surface and move together with it. However, they may form new bonds with other surface atoms of copper and return to the atomic lattice. The above process repeats again and again during sliding, causing a structural change of the copper lattice near the surface, and creating surface roughness of the order of one to three atomic dimensions. In the meantime, some dislocations are also activated in the subsurface (Zhang and Tanaka, 1997).

If δ increases further to its second critical value, $\delta_c^{(2)}$, the above adhering deformation will be replaced by ploughing (Fig. 4.2). An apparent feature of deformation at this stage is that a triangular atom-cluster always exists in front of the leading edge of the diamond asperity and appears as a triangular wave being pushed forward. In this regime, the deformation zone in the subsurface becomes very large and a great number of dislocations are activated. MD simulation, by Zhang and Tanaka also showed the generation of grain boundaries by ploughing.

When δ reaches its third critical value, $\delta_c^{(3)}$, a new deformation state – cutting – appears, characterized by chip formation. Compared with the ploughing regime, the dimension of the deformation zone during cutting is smaller. Dislocations are distributed much more closely to the sliding interface.

Under some specific sliding conditions, not all the regimes would appear except the no-wear regime. For example, if the tip radius of the diamond asperity stays unchanged, but the sliding speed changes, then at lower sliding speeds all four regimes described above will appear. At higher speeds, however, the ploughing regime vanishes; see Fig. 4.3(a). On the other hand, at a given sliding speed, if the tip radius of the asperity is very small, say 1 nm, only the no-wear and

Figure 4.3 Regime transition under specific sliding conditions: (a) non-dimensional indentation depth *vs* sliding speed, (b) non-dimensional indentation depth *vs* tip radius, (c) non-dimensional indentation depth *vs* lubrication/contamination

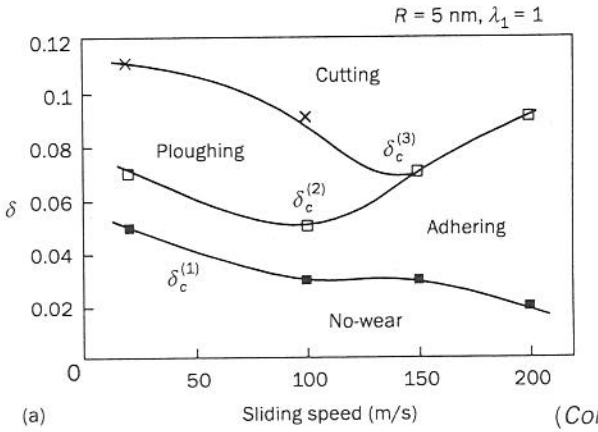

(a)

(*Continued*)

Figure 4.3 *Continued*

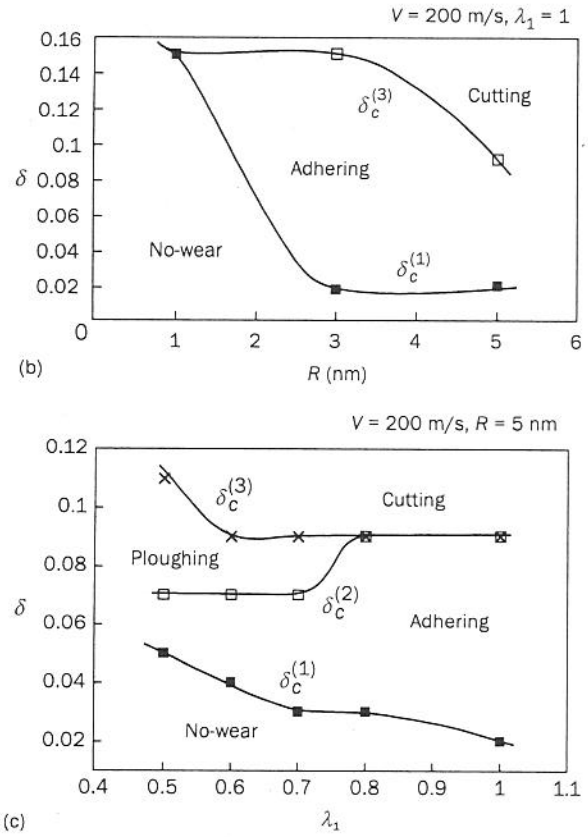

(Reprinted from Zhang and Tanaka (1997) with permission from Elsevier Science.)

cutting regimes emerge, as shown in Fig. 4.3(b). However, with relatively larger tip radii, adhering appears as a transition from no-wear to cutting. Another important factor that alters the deformation transition is the effect of surface lubrication or contamination. If the sliding interface is chemically clean, $\lambda_1 = \lambda_2 = 1$ in eq. [4.1]. In this case, as shown in Fig. 4.3(c), ploughing does not happen at a given sliding speed and tip radius. If the surface is lubricated, $\lambda_1 \leq 1$ with $\lambda_2 \geq 1$, and all the four regimes occur.

It is evident from Fig. 4.3 that the no-wear regime exists in a wide range of indentation depths. In addition, a smaller radius, a lower sliding speed, or better surface lubrication (i.e., smaller λ_1) enlarges the no-wear regime. This strongly indicates that the no-wear design of sliding systems may be realizable in practice. Moreover, it is important to note that the size of the no-wear regime is a strong function of sliding speed and surface lubrication. Therefore, sliding speed and lubrication should be taken into specific account in an attempt to design no-wear sliding systems. Recently, from a carbon-on-copper roller-sliding study, Jeng et al. (2005) reported that minimum resistance at the interface depends on the angular velocity of the roller and the separation distance between the roller and the slab. They found that a negative angular velocity minimizes wear and deformation at the interface.

The formation of various deformation regimes and their transition can be revealed by the variation of temperature distribution and dislocation motion in the atomic lattice. For instance, a larger indentation depth or a higher sliding speed indicates a higher input sliding energy, greater temperature rise and severe plastic deformation. This in turn means a higher density of dislocations with more complicated interactions in the deformed atomic lattice. For detailed information on the MD simulation results of temperature distribution, readers may refer to Zhang and Tanaka (1997).

Frictional behaviour

With the above deformation mechanisms in mind, the frictional behaviour of the system has been analysed. In the cutting regime, the variation of the conventional friction coefficient, $\mu = |F_x/F_y|$, is almost constant with the change of δ, where F_x and F_y are respectively the frictional force and normal indentation force during sliding. Thus it is clear that

in this regime, F_x is proportional to F_y. In other regimes, however, the behaviour of F_x is complex. Particularly, μ becomes singular at a specific δ in the no-wear regime. The singularity of μ can be explained by examining the sliding forces when δ changes. On the atomic scale, the normal sliding force F_y always varies from attractive to repulsive. Thus at the transition point ($F_y = 0$), μ is infinite. The concept of the conventional coefficient of friction is no longer meaningful in the no-wear, adhering and ploughing regimes.

In non-contact sliding, the frictional force can be calculated by using eq. [4.2]. In contact sliding, Zhang and Tanaka obtained the following simple formula in terms of the contact area, based on their theoretical analysis:

$$F_x = \begin{cases} -\sum_{n=1}^{N_d}\sum_{m=1}^{N_c} \frac{\partial}{\partial x_n}\phi(r_{mn}), \text{ for } L_c = 0 \\ \zeta_1^{II} L_c w_a + \zeta_2^{II}, \text{ for } L_c^{(1)} < L_c \le L_c^{(2)} \\ \zeta_1^{III} L_c w_a + \zeta_2^{III}, \text{ for } L_c > L_c^{(2)} \end{cases} \qquad [4.3]$$

where $\zeta_1^{II} = 409$ MPa, $\zeta_2^{II} = 1.807 \times 10^{-8}$ nN, $\zeta_1^{III} = 4.20$ GPa, $\zeta_2^{III} = -1.899$ nN are constants, N_c is the total number of copper atoms in the model, N_d is the number of diamond atoms, L_c is the atomic contact length and $w_a = 0.226$ nm is the width of an atomic layer of copper in the direction perpendicular to its (1 1 1) plane. For $L_c = 0$, F_x is the resultant force of the atomic forces on all the diamond atoms in x-direction and can be derived directly from eq. [4.2]. For $L_c^{(1)} < L_c \le L_c^{(2)}$ and $L_c > L_c^{(2)}$, the empirical expressions given in eq. [4.3] were obtained by fitting the MD simulation data in Fig. 4.4. The physical meaning of product $L_c w_a$ in eq. [4.3] is the atomic contact area in their sliding system. Equation [4.3] and Fig. 4.4, show that the frictional behaviour of an atomic sliding system cannot be described by a single formula.

Figure 4.4 Relationship between the frictional force and contact length

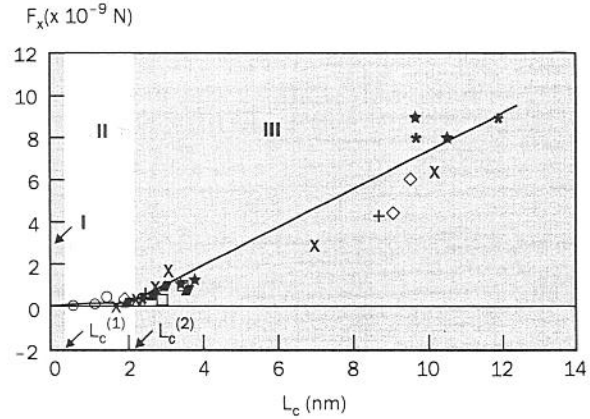

Notes
×: $R = 5$ nm, $V = 20$ m/s, $\lambda_1 = 1$;
*: $R = 5$ nm, $V = 100$ m/s, $\lambda_1 = 1$;
★: $R = 5$ nm, $V = 200$ m/s, $\lambda_1 = 1$;
○: $R = 1$ nm, $V = 200$ m/s, $\lambda_1 = 1$;
◇: $R = 5$ nm, $V = 200$ m/s, $\lambda_1 = 0.5$;
■ $R = 5$ nm, $V = 200$ m/s, $\lambda_1 = 0.6$;
+: $R = 5$ nm, $V = 200$ m/s, $\lambda_1 = 0.7$;
□: $R = 5$ nm, $V = 200$ m/s, $\lambda_1 = 0.8$.

(Reprinted from Zhang and Tanaka (1997) with permission from Elsevier Science.)

There exist two distinct contact sliding zones, Zone II ($L_c^{(1)} < L_c \le L_c^{(2)}$) and Zone III ($L_c > L_c^{(2)}$), where $L_c^{(2)} = 2.216$ nm is the transition boundary from Zones II to III, and $L_c^{(1)} = 0.277$ nm is the minimum contact length defined as the distance between two copper atoms in its (1 1 1) plane. The transition from non-contact to contact sliding is a sudden change because L_c does not exist below $L_c^{(1)}$. In Fig. 4.4, Zone II reflects the frictional behaviour of the system in the no-wear contact sliding, while Zone III shows it in the adhering and ploughing regimes. Thus $L_c^{(2)}$ can be interpreted physically as a critical contact length at which wear takes place. The data scattering in Fig. 4.4 indicates that other variables, such as the tip radius

of asperity R and sliding speed V, also contribute greatly to friction. In other words, F_x should be a function of not only the contact area $L_c w_a$ but also V, R, and so on.

4.3.3 Diamond–silicon sliding systems

Modelling

Let us now consider the two-body and three-body contact sliding problems defined in Fig. 4.1. In the former, asperities are fixed on the sliding surfaces. To understand the fundamental deformation mechanism in a component induced by the penetration of asperities, researchers (Zhang and Tanaka, 1998; Mylvaganam and Zhang, 2009) developed a molecular dynamics model which consisted of a silicon monocrystal work piece in its (1 0 0) plane with thermostat atoms arranged around the control volume to conduct the heat out properly and with boundary atoms arranged fixed to the space to eliminate the rigid body motion. A hemispherical diamond was used as the asperity which should be irregular in reality, but it has been simplified in this study. Since diamond can be considered a rigid body compared with silicon, the model enables one to concentrate on the understanding of the deformation of silicon. In their simulation, Mylvaganam and Zhang used a large portion of the work material having 222,316 Si atoms as the control volume and performed the scratching with a diamond tip of radius 7.5 nm. In three-body contact sliding, the model shown in Zhang and Tanaka (1998) can be used, where the motion of a foreign particle between the two surfaces possesses both a translation and a self-rotation. To facilitate understanding, a single particle is considered for the time being and is approximated by a diamond ball of radius R, moving horizontally (translation) with a speed V_c and in the same time rotating about its centre

independently with a peripheral speed V_r. When $V_r = 0$, the three-body contact sliding reduces to a two-body one. When $V_c = 0$ or $V_r = V_c$, on the other hand, it becomes a pure rolling process. The simulation model for the three-body contact problem used the technique of moving control volume.

Inelastic deformation

The molecular dynamics simulation showed that there always exists a thin layer of amorphous silicon in a specimen subsurface subjected to a two-body contact sliding, as shown in Fig. 4.5(a). This is in agreement with the experimental findings by Zhang and Zarudi (2001) (Fig. 4.5(b)). Gassilloud and co-workers observed nanocrystals embedded within the amorphous silicon when scratching at low speeds (Gassilloud et al., 2005). The thickness of the amorphous layer increases with increasing the penetration depth of asperity, δ. At some critical δ, dislocations can be developed in the crystalline silicon below the amorphous layer (Fig 4.5(c)). The fact that the amorphous layer appears for all δ during sliding shows that on the nanometre scale an inelastic deformation via amorphous phase transformation is a more energetically favourable mechanism. In the case with three-body contact sliding, the mechanism of inelastic deformation is the same, i.e., via amorphous phase transformation. However, because of the kinetic difference in the two-body and three-body sliding motions, the extent of subsurface damage is different. In general, a two-body contact sliding introduces a thinner amorphous layer. A three-body contact sliding, however, may yet leave a perfect crystalline structure after sliding, although wear has happened – this depends on the penetration depth of the particle, the ratio of its 'self-rotation' and 'translation' speeds and variation of atomic bonding strength affected by surface contamination. It was also found that the

Figure 4.5 The subsurface microstructure of silicon monocrystals after a two-body contact sliding (the amorphous phase transformation has been predicted)

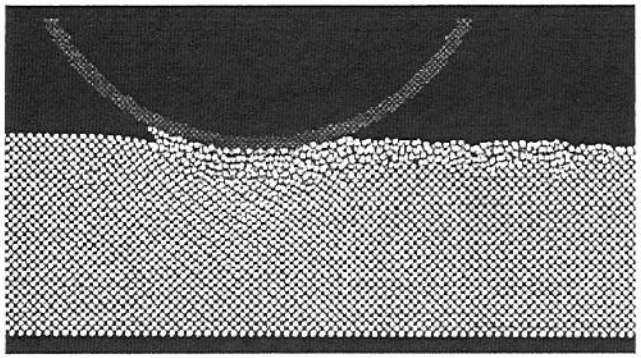

(a) A cross-sectional view of the deformed subsurface of the specimen (V_c=40 m/s, R=7.5 nm, δ=0.5 nm, sliding in [100] direction).

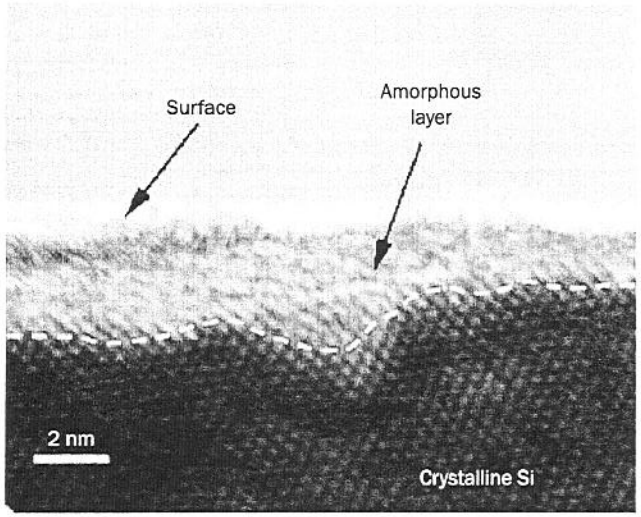

(b) An experimental result of the subsurface damage induced. Note the top amorphous layer (V_c=23.95 m/s, R=1 μm, δ=15.2 nm, sliding in [100] direction). Here, each spot represents a silicon atom.

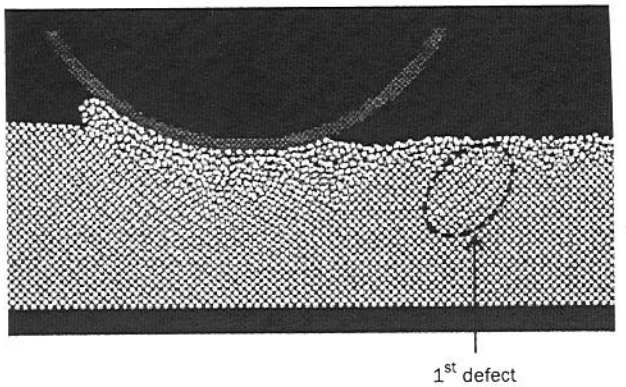

(c) A cross-sectional view of the deformed subsurface of the specimen (V_c=40 m/s, R=7.5 nm, δ=1.0 nm, sliding in [100] direction).

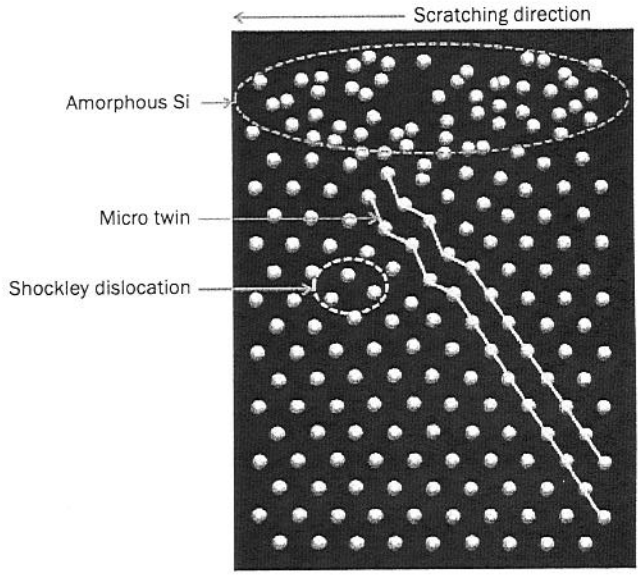

(d) Portion of the atoms on scratching when projected onto (1 1 0) plane showing nano-twin and Shockley dislocation.

(Reprinted from Zhang and Zarudi (2001) with permission from Elsevier Science.)

variation of sliding velocity from 20 m/s to 200 m/s does not change the deformation mechanisms described above.

Defect analysis

In the two-body contact problem, as the penetration depth increases, sliding with the large indenter generated a series of defects/dislocations in the silicon work piece (Fig. 4.5(c)). On analysing a one atomic layer thickness slice in the defect region shown in Fig. 4.5(c) by projecting the atoms on to (1 1 0) plane, showed the presence of nano-twins (Fig. 4.5(d)) with twin plane (1 1 1). The twinning effect stopped at the interior with Shockley partial dislocation located at the front boundaries of the nano-twins. In general, frequent twins and high density of uniform dislocations occur for materials with low stacking fault energy (SFE). Silicon has a low SFE of ~50 mJ/m^2. A very recent Transition Electron Microscopy (TEM) nanoscratch-induced deformation study of single crystal silicon also reported the nucleation of stacking faults and twins (Wu et al., 2009) although the tip radius and the load used in their experiment were much larger compared to those in MD simulation.

Wear regimes

Similar to the wear mechanisms for the diamond–copper sliding system (Zhang and Tanaka, 1997) discussed previously, the wear regimes of the current diamond–silicon system also depend on sliding conditions, as shown by the mechanism diagram Fig. 4.6. In a two-body contact sliding with a given sliding speed, the deformation of a silicon monocrystal falls into a no-wear, adhering, ploughing or cutting regime when the asperity penetration depth varies, as shown in the left half of the figure. Deformation without wear happens only under an extremely small penetration depth, when the atomic

Figure 4.6 The wear diagram (diamond asperities/particles move from right to left; rotation of particles is anticlockwise)

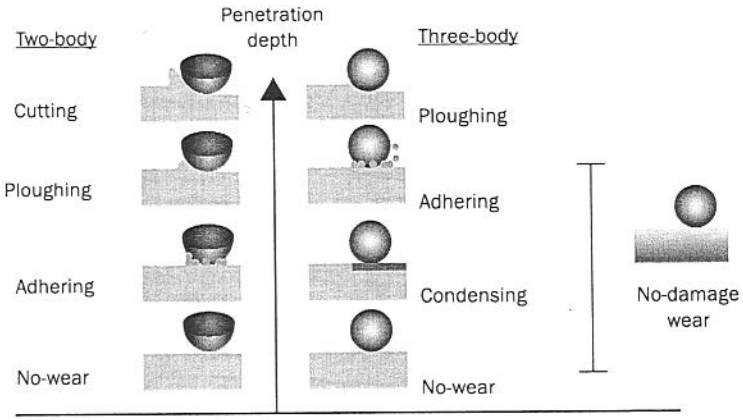

(Reprinted form Zhang and Tanaka (1998) with permission from Elsevier Science.)

lattice of silicon deforms purely elastically. With increasing penetration depth, adhering occurs, in which some surface atoms stick to the asperity surface and move together with it to cause wear. However, these atoms may return to the silicon substrate during sliding if the specimen surface has not been contaminated. When the penetration depth increases further, a new wear state, ploughing, characterized by an atomic cluster being pushed to move with the asperity, will appear. A further increase of the penetration depth leads to a continuous cutting process where the penetration depth of the asperity and the impingement direction has significant influence on the phase transformation and dislocation (Mylvaganam and Zhang, 2009).

In a three-body contact sliding, however, silicon will experience different wear regimes. They are the no-wear, condensing, adhering and ploughing regimes, as shown in the right half of Fig. 4.6. After the pure elastic deformation in the no-wear regime, the amorphous phase under the

particle will experience a remarkable condensing locally without material removal. In other words, because the density of the surface silicon atoms under particle indentation becomes higher, condensing creates a sliding mark on the specimen surface. Thus condensing is a special wear process without material removal. A further particle penetration will lead to adhering and ploughing. These regimes are similar to the corresponding ones in the two-body contact sliding. Cutting rarely happens in three-body sliding processes but is possible if the particle penetration depth becomes sufficiently large and the self-rotation speed becomes small.

Another interesting phenomenon associated with the three-body contact sliding is the existence of a regime of no-damage wear. Under certain sliding conditions, the atomic bonding strength among surface silicon atoms can be weakened chemically. When this happens, these atoms can be removed via adhesion because diamond–silicon attraction is still strong. Due to the re-crystallization behind the particle, a worn specimen may appear as damage-free in the majority of its subsurface with only a little distortion within one or two surface atomic layers. In conjunction with the phenomenon that occurred in the condensing regime discussed above, it becomes obvious that a perfect subsurface after a three-body contact sliding does not necessarily indicate a no-wear process.

4.3.4 Effects of contact size and multiple asperities

Contact size

The investigation on diamond–copper sliding (Zhang and Tanaka, 1997), described in section 4.3.2, focused on the friction and wear mechanisms when the radius of the asperity

R is a constant while the depth of asperity indentation δ increases. Wear and plastic deformation consequently occur when δ reaches a critical value.

Based on some experimental observations (Carpick et al., 1996; Lantz et al., 1997), Hurtado and Kim (1999) proposed a micro-mechanical dislocation model of frictional slip, predicting that when the contact size is small the friction stress is constant and of the order of the theoretical shear strength. This is in agreement with AFM friction experiments. However, at a critical contact size there is a transition beyond which the frictional stress decreases with increasing contact size, until it reaches a second transition where the friction stress gradually becomes independent of the contact size. Hence, the mechanisms of slip are size-dependent, or in other words, there exists a scale effect. Before the first transition, the constant friction is associated with concurrent slip of the atoms without the aid of dislocation motion. The first transition corresponds to the minimum contact size at which a single dislocation loop is nucleated and sweeps through the whole contact interface, resulting in a single-dislocation-assisted slip. This mechanism is predicted to prevail for a wide range of contact sizes, from 10 nm to 10 μm, in radius for typical dry adhesive contacts. The second transition occurs for contact sizes larger than 10 μm, beyond which friction stress is once again constant due to cooperative glide of dislocations within dislocation pileups. The above dislocation model excludes wear or plastic deformation of the sliding parts.

To clarify this issue, Zhang et al. (2001) carried out a nano-tribology analysis using molecular dynamics by varying the asperity radius from 5 nm to 30 nm and keeping the indentation depth unchanged. The model consists of a single cylindrical asperity (rigid diamond) of various radii, sliding across a copper (1 1 1) plane with a speed of 5 m/s. The indentation depth, d, was 0.46 nm and −0.14 nm (0.14 nm

above the work piece), respectively, where d is the distance between the surfaces of the asperity and specimen defined by the envelopes at the theoretical radii of their surface atoms. It must be noted that the molecular dynamics simulation cannot capture the second transition because it will require too long a computation time to analyse a model in the order of micrometres.

In the simulations where the asperity penetration depths are small enough so that there are no dislocations created within copper, the deformation corresponds to the no-wear regime described by Zhang and Tanaka (1997). In the case where the radius of the diamond asperity is less than 12 nm, the carbon atoms slide across the copper atoms in close contact. The surface of the copper work piece conforms closely to the shape of the asperity tip in contact (Fig. 4.7(a)). The variation of force with time steps showed strong indication of atomic stick-slip between the atoms of the asperity and the work piece. This implies that the sliding mechanism involved is similar to the ideal slip of two atomic planes in a perfect dislocation-free crystal. Hurtado and Kim (1999) referred to this sliding mechanism as concurrent slip.

When the asperity radius exceeds 12 nm, there are considerable differences in the sliding mechanism involved. The surface of the copper work piece does not conform closely to the shape of the carbon asperity (Fig. 4.7(b)) and the force variation shows little atomic stick-slip between the atoms of the asperity and the work piece. In addition, the friction stress is constant before the first transition but after which it decreases with the increasing contact width (Fig. 4.8). This figure further shows the indentation depth influences both the critical contact size at which first transition occurs and the rate of friction reduction after the transition. All these observations clearly indicate a change in the mechanism of sliding as predicted by Hurtado and

Figure 4.7 Diamond asperity sliding on a monocrystalline copper surface

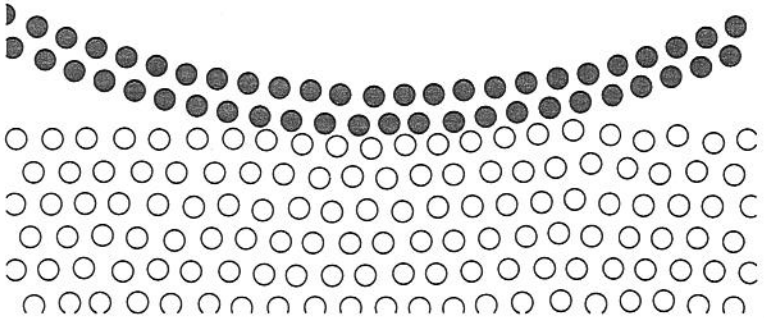

(a) Radius 8 nm – surface of copper workpiece conforms closely to shape of asperity with good contact.

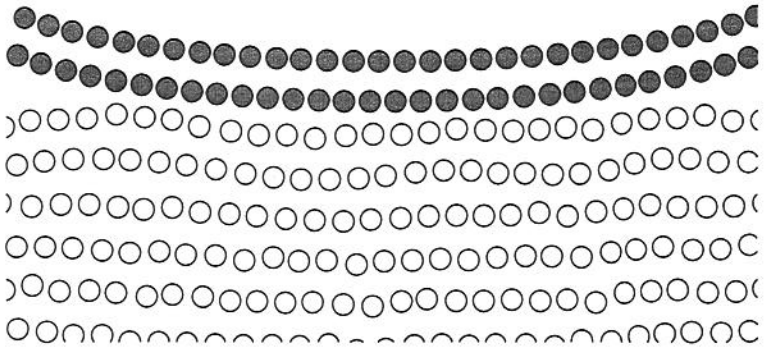

(b) Radius 30 nm – surface of copper workpiece does not conform closely to the shape of the asperity

(Reprinted from Zhang et al. (2001) with permission from Springer Publishers.)

Kim. However, at the greater indentation depth, permanent damage and wear occurred. Dislocation lines indicating plastic deformation 'within the body of the solid' are visible. This behaviour is similar to the adhering regime described by Zhang and Tanaka (1997).

Although in the MD simulation described above, only the first transition was observed, the fact that the friction stress decreases after this indicates that the coefficient of friction

Figure 4.8 Frictional stress *vs* contact width for indentation depths of −0.14 nm and 0.46 nm

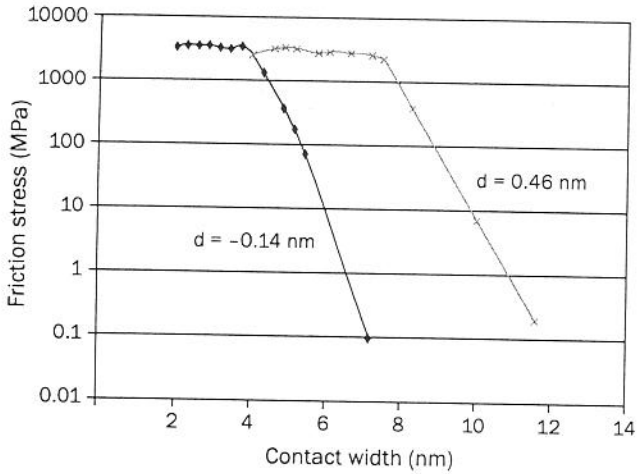

(Reprinted from Zhang et al. (2001) with permission from Springer Publishers.)

could change between the first and second transition. Thus in the experiment, depending on the probe radius and the load used, if the contact width falls within this region it is possible to get a different coefficient of nano-scale friction compared to macro-scale friction as observed in the latter part of section 4.2.3.

The contact width between the asperity and work piece obtained by the above molecular dynamics simulation can be compared with the predictions of the JKR theory (Johnson, 1985; Johnson et al., 1971) which shows that – for the present configuration of a circular cylinder in contact with a half space (plane-strain) – the indentation load per unit width on the asperity, P, and the contact width, 2a, follows the relationship

$$P = \frac{\pi E^* a^2}{4R} - \sqrt{2\pi E^* a w}, \qquad [4.4]$$

where R is the radius of the asperity, E^* is the effective modulus of the contact system (Johnson, 1985), w is the work of adhesion and can be determined by a nano-indentation simulation using molecular dynamics analysis. It is found that for the present diamond–copper (C–Cu) system, $w_{C\text{-}Cu} = 1.476\,\text{J/m}^2$. Since the diamond asperity is assumed to be a rigid body, the E^* in eq. [4.4] becomes 125.36 GPa by taking $E_C = \infty$, $E_{Cu} = 110\text{GPa}$ and $\nu_{Cu} = 0.35$ (Callister, 1995).

Table 4.3 compares the contact widths from the molecular dynamics simulation, the JKR theory of eq. [4.4] and the Hertzian contact theory under various conditions. The values from the JKR and simulation are different, although the deformation of the copper work piece at $d = -0.14\,\text{nm}$ was purely elastic and that at $d = 0.46\,\text{nm}$ was almost purely inelastic. A possible cause is that the contact width of the molecular dynamics simulation contains the effect of sliding, while eq. [4.4] does not. It is also worth noting that compared to the predictions by the Hertzian contact theory, the

Table 4.3 Contact lengths by the JKR and MD analyses for the case of diamond–copper interactions

	Contact length 2a (nm)		
		$d = -0.14\,\text{nm}$, $P = 0.625\,\text{N/m}$	$d = 0.46\,\text{nm}$, $P = 22.969\,\text{N/m}$
$R = 5\,\text{nm}$	JKR	2.914	3.764
	MD	2.870	4.120
	Hertz	0	2.160
		d = −0.14 nm, P = 0.824 N/m	d = 0.46 nm, P = 27.34 N/m
$R = 8\,\text{nm}$	JKR	3.99	5.152
	MD	3.731	5.740
	Hertz	0	2.980

predictions by the JKR theory is much closer to the molecular dynamics results. This indicates that the effect of normal adhesion is considerable.

Sliding by multi-asperities

The single sliding asperity study has provided us with important knowledge on the deformation mechanisms of friction and wear of monocrystalline materials. In a real sliding system, however, a counterpart material is actually subjected to multi-asperity interactions, as illustrated in Fig. 4.1(a) and 4.1(b). When the first asperity has created a damaged zone, the material may deform differently under subsequent sliding interactions. Cheong and Zhang (2003) thus discussed the effects of the sliding by multi-asperities.

The mechanics model consists of three spherical diamond asperities, A, B and C, sliding on an atomically smooth silicon surface, as illustrated in Fig. 4.9. Their relative positions and orientations are defined by their distances, L_{AB} and L_{AC}, and angles with respect to the sliding direction, α and θ. There are three cases of special interest: (I) $\alpha=\theta=0°$ with $L_{AB}<L_{AC}$, representing a repeated single-asperity sliding so that the effect of residual subsurface

Figure 4.9 The mechanics model for multi-asperity contact sliding

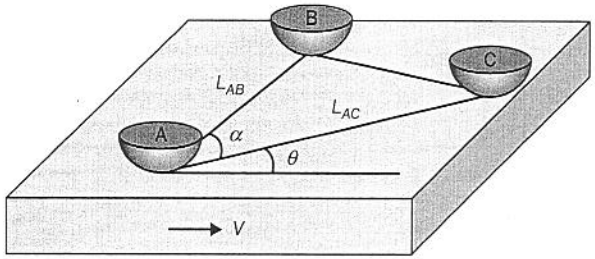

(Reprinted from Cheong and Zhang (2003) with permission from Interscience Publishers.)

damage can be understood; (II) $\alpha=0°$ and $\theta=90°$ with $L_{AB}=L_{AC}$, standing for the interaction of two parallel asperities; and (III) $\alpha=90°$ and $\theta=0°$, indicating the case with parallel sliding asperities coupled with an interaction from a third asperity. Again, since diamond is much harder than silicon, the asperities are modelled as rigid spheres. These spheres slide across the silicon surface at a specified velocity 40 m/s. The maximum depth of asperity penetration is 1.0 nm.

Case I

In this case, the second and third asperities B and C retrace the damaged path caused by asperity A, as in Fig. 4.10. Therefore, the cutting mechanism involved in the first and the following two asperities are very different. Asperity A cuts the silicon work piece in the same fashion as the case of a single sliding asperity, causing phase transformation of the original diamond cubic silicon. Asperity B, however, ploughs through the residual amorphous layer in the wake of asperity A. Again β-tin silicon forms beneath the asperity and then transforms into amorphous silicon when the asperity passes showing that the β-tin silicon phase is recoverable from the amorphous phase, provided that the required stress field is achieved. However, only some of the β-tin silicon is

Figure 4.10 Cross-sectional view of silicon work piece and asperities A, B and C during sliding as in case I

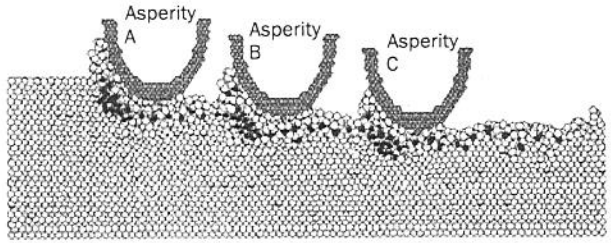

(Reprinted from Cheong and Zhang (2003) with permission from Interscience Publishers.)

recovered as asperities B and C retrace the amorphous damaged zone.

Cases II and III

In these cases, the asperities do not retrace the damaged zones. At the depth of asperity penetration of 1.0 nm, the wear mechanism observed is that of cutting and the plastic deformation due to the sliding asperities is very much localized. Figure 4.11 shows a cross-section of the silicon work piece through the centre of the asperities and it can be seen that there is almost no subsurface damage to the work piece between the two asperities. Localized plastic deformation occurs beneath the asperities.

The sliding asperities A, B and C also create trails of amorphous silicon within subsurface layers in the damaged zones, just as in nano-indentation (Cheong and Zhang, 2000). This is because, as the asperity slides across the silicon work piece, diamond cubic silicon continuously transforms into β-tin silicon beneath the asperity and then transforms into amorphous silicon when the asperity passes, leaving a layer of subsurface amorphous silicon in its wake.

Figure 4.11 Cross-section of the silicon workpiece through the centre of asperities (cases II and III)

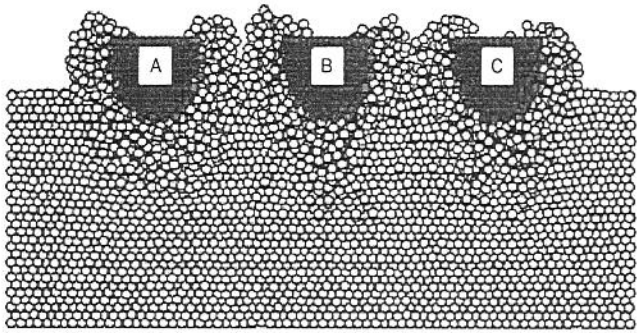

(Reprinted from Cheong and Zhang (2003) with permission from Interscience Publishers.)

Dislocations are absent at this particular depth of asperity penetration. This suggests that the plastic deformation is solely due to phase transformation.

4.4 Summary

This chapter has briefly discussed some fundamentals in studying the micro/nano-tribological properties such as adhesion, wear and friction using experimental techniques such as SFA, STM and AFM/FFM and the molecular dynamics technique. These techniques have different capabilities. In SFA the atomically smooth surface probe has a large contact area. This helps to have a film of uniform thickness between the two surfaces. In AFM, the sharp tip has a small contact area making it difficult to measure the film thickness and exact contact size, but it is capable of measuring the nano-tribological properties of any substrate.

The theoretical investigations using the MD technique have shown that in an atomic sliding system there generally exist four regimes, namely the no-wear regime, adhering regime, ploughing regime and cutting regime. The transition between different deformation regimes are governed by tip penetration depth, sliding speed, asperity geometry, and surface lubrication conditions. A smaller tip radius or a smaller sliding speed can bring about a greater no-wear regime. In addition, MD studies showed that a friction transition takes place at a critical contact size.

4.5 Note

1. Here, $12{,}000 \leq N \leq 15{,}000$ is used in conjunction with the technique of moving control volume.

4.6 References

Becker, R. S., Golovchenko, J. A., Hanmann, D. R. and Swartzentruber, B. S. (1985), 'Real-space observation of surface states on si(111) 7×7 with the tunnelling microscope', *Physical Review Letters* 55: 2032–4.

Bhushan, B. (1995), 'Micro/nanotribology and its applications to magnetic storage devices and mems', *Tribol. Int.* 28: 85–95.

Bhushan, B. (2005), 'Nanotribology and nanomechanics', *Wear* 259: 1507–31.

Bhushan, B. and Dandavate, C. (2000), 'Thin-film friction and adhesion studies using atomic force microscopy', *J. Appl. Phys.* 87: 1201–10.

Bhushan, B. and Ruan, J. (1994), 'Atomic scale friction measurements using friction force microscopy. Part ii. Application to magnetic media', *ASME J. Trib.* 116: 389–96.

Bhushan, B. and Sundararajan, S. (1998), 'Micro/nanoscale friction and wear mechanisms of thin films using atomic force and friction force microscopy', *Acta Mater.* 46: 3793–804.

Binnig, G., Quate, C. F. and Gerber, C. (1986), 'Atomic force microscope', *Physical Review Letters* 56: 930–3.

Binning, G., Rohrer, H., Gerber, C. and Weibel, E. (1982), 'Surface studies by scanning tunneling microscopy', *Physical Review Letters* 49: 57–61.

Bowden, F. P. and Tabor, D. (1967), *Friction and Lubrication*, London: Methuen.

Callister, W. D. Jr. (1995), *Materials Science and Engineering – An Introduction*, New York: John Wiley & Sons.

Carpick, R. W., Agrait, D. F., Ogletree, D. F. and Salmeron, M. (1996), 'Variation of the interfacial shear strength and adhesion of a nanometer-sized contact', *Langmuir* 12: 505.

Cheong, W. C. D. and Zhang, L. C. (2000), 'Molecular dynamics simulation of phase transformations in silicon monocrystals due to nano indentation', *Nanotechnology* 11: 173.

Cheong, W. C. D. and Zhang, L. C. (2003), 'A stress criterion for the β-sn transformation in silicon under indentation and uniaxial compression', *Key Engineering Materials* 233–236, 603.

Cheong, W. C. D. and Zhang, L. C. (2003), 'Monocrystalline silicon subjected to multi-asperity sliding: nano-wear mechanisms, subsurface damage and effect of asperity interaction', *Int. J. Materials & Product Tech.* 18: 398.

Cheong, W. C. D., Zhang, L. C. and Tanaka, H. (2001), 'Some essentials of simulating nano-surfacing processes using the molecular dynamics method', *Key Engineering Materials* 196: 31.

Courtney, T. H. (1990), *Mechanical Behaviour of Materials*, Singapore: McGraw-Hill.

Eigler, D. M. and Schweizer, E. K. (1990), 'Positioning single atoms with a scanning tunneling microscope', *Nature* 344: 524–6.

Foster, J. S., Frommer, J. E. and Arnett, P. C. (1988), 'Molecular manipulation using a tunnelling microscope', *Nature* 331: 324–6.

Gassilloud, R., Ballif, C., Gasser, P., Buerki, G. and Michler, J. (2005), 'Deformation mechanisms of silicon during nanoscratching', *Applications and Materials Science* 202: 2858–69.

Homola, A. M., Israelachvili, J. N., McGuiggan, P. M. and Gee, M. L. (1990), 'Fundamental experimental studies in tribology – the transition from interfacial friction of

undamaged molecularly smooth surfaces to normal friction with wear', *Wear* 136: 65–83.

Hurtado, J. A. and Kim, K-S. (1999), 'Scale effects in friction of single asperity contacts. Ii. Multiple-dislocation-cooperated slip', *Proc. R. Soc. London A* 455: 3363.

Israelachvili, J. N. and Tabor, D. (1972), 'The measurement of van der waals dispersion forces in the range of 1.5 to 130 nm', *Proc. R. Soc. London A* 331: 19–38.

Jeng, Y-R., Tsai, P-C. and Fang, T-H. (2005), 'Molecular dynamics studies of atomic-scale friction for roller-on-slab systems with different rolling-sliding conditions', *Nanotechnology* 16: 1941–9.

Johnson, K. L. (1985), *Contact Mechanics*, Cambridge: Cambridge University Press.

Johnson, K. L., Kendall, K. R. and Roberts, A. D. (1971), 'Surface energy and the contact of elastic solids', *Proc. R. Soc. London A* 324: 301.

Kaneko, R., Nonaka, K. and Yasuda, K. (1988), 'Scanning tunneling microscopy and atomic force microscopy for microtribology', *J. Vac. Sci. Tech.* A6: 291.

Kendall, K. (1994), 'Adhesion: molecules and mechanics', *Science* 263: 1720–5.

Koinkar, V. N. and Bhushan, B. (1997), 'Effect of scan size and surface roughness on microscale friction measurements', *J. Appl. Phys.* 81: 2472–9.

Lantz, M. A., O'Shea, S. L., Welland, M. E. and Johnson, K. L. (1997), 'Atomic-force-microscope study of contact area and friction on $nbse_2$', *Phys. Rev. B* 55: 10776.

Mate, C. M., McClelland, G. M., Erlandsson, R. and Chiang, S. (1987), 'Atomic-scale friction of a tungsten tip on a graphite surface', *Physical Review Letters* 59: 1942–5.

McGuiggan, P. M., Zhang, J. and Hsu, S. M. (2001), 'Comparison of friction measurements using the atomic force microscope and the surface forces apparatus: the issue of scale', *Tribol. Lett.* 10: 217–23.

Mylvaganam, K. and Zhang, L. C. (2009), 'Nanoscratching-induced phase transformation of monocrystalline silicon – the depth-of-cut effect', *Adv. Mat. Res.* 76–78: 387–91.

Ruan, J. and Bhushan, B. (1994), 'Atomic-scale and microscale friction of graphite and diamond using friction force microscopy', *J. Appl. Phys.* 76: 5022–35.

Ruan, J. and Bhushan, B. (1994), 'Atomic-scale friction measurements using friction force microscopy: Part i general principles and new measurement technique', *ASME J Tribol.* 116: 378–88.

Sundararajan, S. and Bhushan, B. (2000), 'Topography induced contributions to friction forces measured using an atomic force/friction force microscope', *J. Appl. Phys.* 88: 4825–31.

Tabor, D. and Winterton, R. H. S. (1969), 'The direct measurement of normal and retarded van der waals forces', *Proc. R. Soc. Lond. A* 312: 435–50.

Tanaka, H. and Zhang, L. C. (1996), in *Progress of Cutting and Grinding*, ed N Narutaki, Osaka: Japan Society for Precision Engineering, p. 262.

Wu, Y. Q., Huang, H., Zou, J. and Dell, J. M. (2009), 'Nanoscratch-induced deformation of single crystal silicon', *Journal of Vacuum Science & Technology B* 27: 1374–7.

Zarudi, I., Cheong, W. C. D., Zou, J. and Zhang, L. C. (2004), 'Atomistic structure of monocrystalline silicon in surface nano-modification', *Nanotechnology* 15: 104.

Zhang, L. C. and Tanaka, H. (1997), 'Towards a deeper understanding of wear and friction on the atomic scale-a molecular dynamics analysis', *Wear* 211: 44–53.

Zhang, L. C. and Tanaka, H. (1998), 'Atomic scale deformation in silicon monocrystals induced by two-body

and three-body contact sliding', *Tribol. Int.* 31: 425–33.

Zhang, L. C. and Tanaka, H. (1999), 'On the mechanics and physics in the nano-indentation of silicon monocrystals', *JSME Int. J. Series A* 42: 546–59.

Zhang, L. C. and Zarudi, I. (2001), 'Towards a deeper understanding of plastic deformation in mono-crystalline silicon', *Int. J. Mech. Sci.* 43: 1985–96.

Zhang, L. C., Johnson, K. L. and Cheong, W. C. D. (2001), 'A molecular dynamics study of scale effects on the friction of single-asperity contacts', *Tribol. Lett.* 10: 23.

Zhao, X. and Bhushan, B. (1998), 'Material removal mechanism of single-crystal silicon on nanoscale and at ultra-low loads', *Wear* 223: 66–78.

Tribology in manufacturing

M. Jackson, Purdue University, USA and J. Morrell, Y12 National Security Complex, USA

Abstract: This chapter focuses on tribology in manufacturing processes from the viewpoint of understanding the fundamentals of sliding friction in those processes and the use of lubricants to control friction in manufacturing processes such as machining, drawing, rolling, extrusion, abrasive processes and processing at the micro and nanoscales. It is assumed that this chapter will serve as a focal point for engineers who are concerned with the role of tribology to maximize productivity and reduce costs associated with manufacturing processes under their command.

Keywords: tribology, manufacturing, lubrication, wear, friction.

5.1 Friction in manufacturing

The nature of the contact between surfaces is an important aspect of understanding the function of tribology in manufacturing processes, so macrocontacts and the stresses